A&A 491, 455–464 (2008)
DOI: 10.1051/0004-6361:200810432

Astronomy & Astrophysics

Ram-pressure stripped molecular gas in the Virgo spiral galaxy NGC 4522[⋆]

B. Vollmer[1], J. Braine[2], C. Pappalardo[1], and P. Hily-Blant[3]

[1] CDS, Observatoire astronomique de Strasbourg, 11 rue de l'université, 67000 Strasbourg, France
e-mail: `bvollmer@astro.u-strasbg.fr`
[2] Laboratoire d'Astrophysique de Bordeaux (OASU), Université de Bordeaux, UMR 5804, CNRS/INSU, BP 89, 33270 Floirac, France
[3] IRAM, Domaine Universitaire, 300 rue de la Piscine, 38406 Saint-Martin d'Hères, France

Received 20 June 2008 / Accepted 17 September 2008

ABSTRACT

IRAM 30 m ^{12}CO(1–0) and ^{12}CO(2–1) HERA observations are presented for the ram-pressure stripped Virgo spiral galaxy NGC 4522. The CO emission is detected in the galactic disk and the extraplanar gas. The extraplanar CO emission follows the morphology of the atomic gas closely but is less extended. The CO maxima do not appear to correspond to regions where there is peak massive star formation as probed by Hα emission. The presence of molecular gas is a necessary but not sufficient condition for star formation. Compared to the disk gas, the molecular fraction of the extraplanar gas is 30% lower and the star formation efficiency of the extraplanar gas is about 3 times lower. The comparison with an existing dynamical model extended by a recipe for distinguishing between atomic and molecular gas shows that a significant part of the gas is stripped in the form of overdense arm-like structures. It is argued that the molecular fraction depends on the square root of the total large-scale density. Based on the combination of the CO/Hα and an analytical model, the total gas density is estimated to be about 4 times lower than that of the galactic disk. Molecules and stars form within this dense gas according to the same laws as in the galactic disk, i.e. they mainly depend on the total large-scale gas density. Star formation proceeds where the local large-scale gas density is highest. Given the complex 3D morphology this does not correspond to the peaks in the surface density. In the absence of a confining gravitational potential, the stripped gas arms will most probably disperse; i.e. the density of the gas will decrease and star formation will cease.

Key words. galaxies: individual: NGC 4522 – galaxies: interactions – galaxies: ISM – galaxies: kinematics and dynamics – stars: formation – radio lines: ISM

1. Introduction

The best-studied case of active ram-pressure stripping of a cluster galaxy is NGC 4522 located in the Virgo cluster. Only in this cluster is the resolution of radio telescopes sufficient (~20″ = 1.6 kpc[1]) for a detailed analysis of the gas morphology and kinematics. NGC 4522 is a rather small (D_{25} = 4′ = 20 kpc) edge-on Sc galaxy with a rotation velocity of ~100 km s^{-1}. It is strongly HI deficient (DEF = 0.6; Helou et al. 1984). Its projected distance to the cluster center (M 87) is large (~1 Mpc), and its radial velocity with respect to the Virgo cluster mean is high (1150 km s^{-1}). HI and Hα observations (Kenney et al. 2004; Kenney & Koopmann 1999) show a heavily truncated gas disk at a radius of 3 kpc, which is ~40% of the optical radius, and a significant amount of extraplanar gas to the west of the galactic disk. The one-sided extraplanar atomic gas distribution shows high column densities, comparable to those of the adjacent galactic disk. The 6 cm polarized radio continuum emission shows a maximum at the eastern edge of the galactic disk, on the opposite side of the extraplanar gas and star formation. Since the stellar disk is symmetric and undisturbed (Kenney & Koopmann 1999), a tidal interaction is excluded as the origin of the peculiar gas distribution of NGC 4522. Thus, this galaxy undergoes ram-pressure stripping due to the galaxy's rapid motion within the hot and tenuous intracluster gas (ICM) of the Virgo cluster.

Vollmer et al. (2006) made a dynamical model that includes the effects of ram pressure for NGC 4522. The model successfully reproduces the large-scale gas distribution and the velocity field. By assuming a Gaussian distribution of relativistic electrons, they obtained the distribution of polarized radio continuum emission, which reproduces the VLA observations of polarized radio continuum emission at 6 cm. The observed maximum of the polarized radio continuum emission is successfully reproduced. The eastern ridge of polarized radio continuum emission is therefore due to ram pressure compression of the interstellar medium (ISM) and its magnetic field. The dynamical model and the analysis of the stellar populations of the outer gas-free disk using optical spectra and UV photometry (Crowl & Kenney 2006) indicate that the ram pressure maximum occurred only ~50–100 Myr ago. This scenario has one important caveat: the large projected distance of NGC 4522 (1 Mpc) to the center of the Virgo cluster (M 87). Assuming a static smooth ICM and standard values for the ICM density and the galaxy velocity, the ram pressure at that location seems to be too low by an order of magnitude to produce the observed truncation of the gas disk. A natural explanation for the enhanced ram pressure efficiency is that the intracluster medium is not static but moving due to the infall of the M 49 group of galaxies from behind (Kenney et al. 2004; Vollmer et al. 2004; Vollmer et al. 2006). In this case the

---

[⋆] Based on IRAM 30 m HERA observations.

[1] We use a distance of 17 Mpc for the Virgo cluster.

galaxy has just passed the region of highest intracluster medium velocity.

While we know from the Hα observations (Kenney et al. 2004; Kenney & Koopmann 1999) that stars are forming in the extraplanar gas, we do not know the distribution of molecular gas in these regions. How does the complex multiphase interstellar medium respond to ram pressure stripping? Can we model the molecular gas content during the interaction using simplified recipes? Can dense molecular gas decouple from the ram pressure wind as suggested for NGC 4438 (Vollmer et al. 2005)? In this article we present IRAM 30 m ^{12}CO(1–0) and ^{12}CO(2–1) HERA observations of NGC 4522 to investigate the fate of the stripped gas.

We present our CO observations in Sect. 2 followed by the observational results in Sect. 3. The detection of ram pressure wind decoupled molecular clouds is reported in Sect. 4. In Sect. 5 we compare our CO observations to existing HI and Hα emission distributions (Kenney et al. 2004) and to the dynamical model of Vollmer et al. (2006). The molecular fraction and star formation efficiencies are discussed in Sect. 6 and we give our conclusions in Sect. 7.

2. Observations

The observations of the CO(1–0) and CO(2–1) lines, with rest frequencies of 115.271204 and 230.53799 GHz respectively, were carried out at the 30 m millimeter-wave telescope on Pico Veleta (Spain) run by the Institut de RadioAstronomie Millimétrique (IRAM). The CO(2–1) observations used the HERA multi-beam array, with 3 × 3 dual-polarization receivers, and the WILMA autocorrelator backend with 2 MHz spectral resolution. The CO(1–0) observations used the single-pixel "AB" receivers and the 1 MHz filterbanks as backends. The spectral resolution is 2.6 km s^{-1} in both cases. The HERA observations were made in February and March 2006 and the CO(1–0) in November 2006. In both cases, a nutating secondary ("wobbler") was used with a throw of 180–200 arcsec in order to be clear of any emission from the galaxy. The positions observed in each line are indicated in Figs. 1 and 2 as triangles for CO(2–1) and circles for CO(1–0).

Data reduction was straightforward, eliminating any obviously bad channels and excluding the spectra taken under particularly poor conditions (system temperature over 1000 K). Spectra were then summed position by position. System temperatures of the final spectra ranged from 200 to 500 K on the Ta* scale. All spectra are presented on the main beam temperature scale, assuming telescope main-beam and forward efficiencies of $\eta_{\rm mb} = 0.54$ and $\eta_{\rm for} = 0.90$ for HERA and $\eta_{\rm mb} = 0.74$ and $\eta_{\rm for} = 0.95$ for the CO(1–0) line. The spectra near map edges with noise levels greater than 28 mK ($T_{\rm mb}$ scale) are left out of Fig. 2. At the assumed distance of NGC 4522, 17 Mpc, the CO(2–1) and CO (1–0) beams correspond to 0.9 and 1.7 kpc respectively. In order to convert CO integrated intensities into molecular gas masses, we have assumed a $N({\rm H_2})/I_{\rm CO(2-1)}$ ratio of 2×10^{20} H$_2$ mol cm^{-2} per K km s^{-1}. Our conclusions, however, do not depend strongly on the $N({\rm H_2})/I_{\rm CO}$ ratio within reasonable variations.

3. Disk and extraplanar molecular gas

3.1. CO spectra

Figures 3–6 show the ^{12}CO(2–1) HERA spectra (resolution of 11″) together with the HI spectra of Kenney et al. (2004; resolution of 20″) and the model HI and CO emission convolved to the observational resolutions (see Sect. 5). We observe that the HI emission is more extended than the CO emission. Where detected, the velocity of the CO lines are close to the HI velocities. In general, CO linewidths are comparable to the HI linewidths in the galactic disk (Fig. 4), but smaller in the extraplanar regions (Figs. 3, 6). A double-line profile is observed in the CO and HI line west of the galaxy center at offsets (−23, 0), (−23, 8) (Fig. 5). This kind of line-profile has also been observed in NGC 4438 (Vollmer et al. 2005) another Virgo spiral galaxy which undergoes ram pressure stripping together with a tidal interaction. In the southwestern part of the extraplanar gas the HI profiles show a blueshifted wing (Fig. 6), corresponding to the most strongly pushed gas. Whereas the CO peak in this region is aligned with the HI peak, the blueshifted wing is absent in CO. This might be partly due to the smaller S/N ratio of the CO data compared to the HI data. Even if there is H$_2$ associated with the blueshifted wing, we can conclude that the molecular fraction in this extraplanar gas is lower in the blueshifted wing than in the main line.

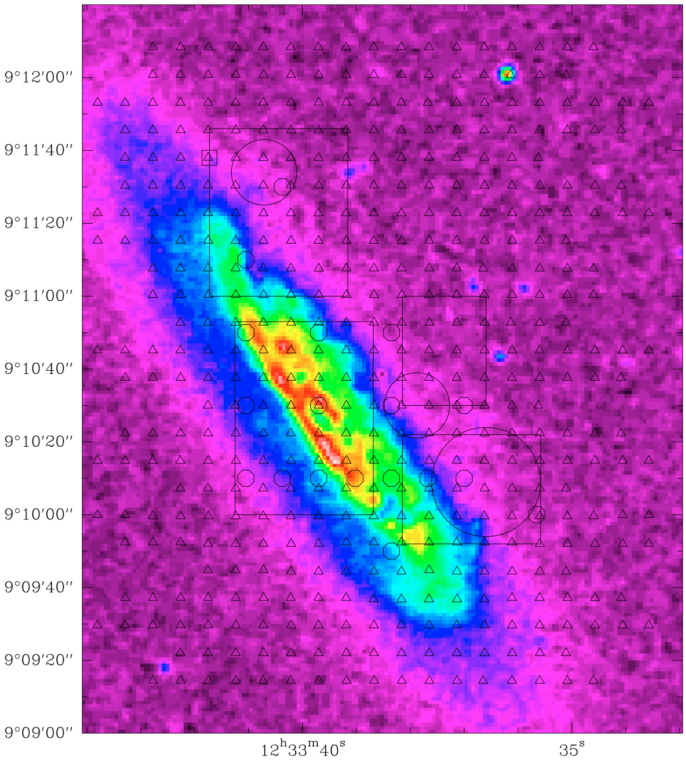

Fig. 1. IRAM 30 m pointings on a DSS *B* band image. Triangles: ^{12}CO(2–1) HERA observations. Small circles: ^{12}CO(1–0) observations. Large circles: Binned HERA pointings (see Fig. 7). The large boxes correspond to Figs. 3 to 6.

Figure 7 shows ^{12}CO(2–1) HERA spectra of selected regions (large circles in Figs. 1, 2). To obtain a better S/N ratio, the HERA spectra within each region were averaged. These selected regions show the following characteristics:

- CO emission is present in the northwestern extraplanar gas at offset (15″, 64″). The line is redshifted by ~20 km s^{-1} with respect to the HI line (Fig. 7 left panel).
- The double profile observed in the HI line at offset (−27″, 0) is also present in the CO line. The CO and HI peak amplitudes and their separation are the same (Fig. 7 middle panel).
- In the southwestern extraplanar gas at offset (−46″, −21″) the blueshifted wing of the HI line profile has no

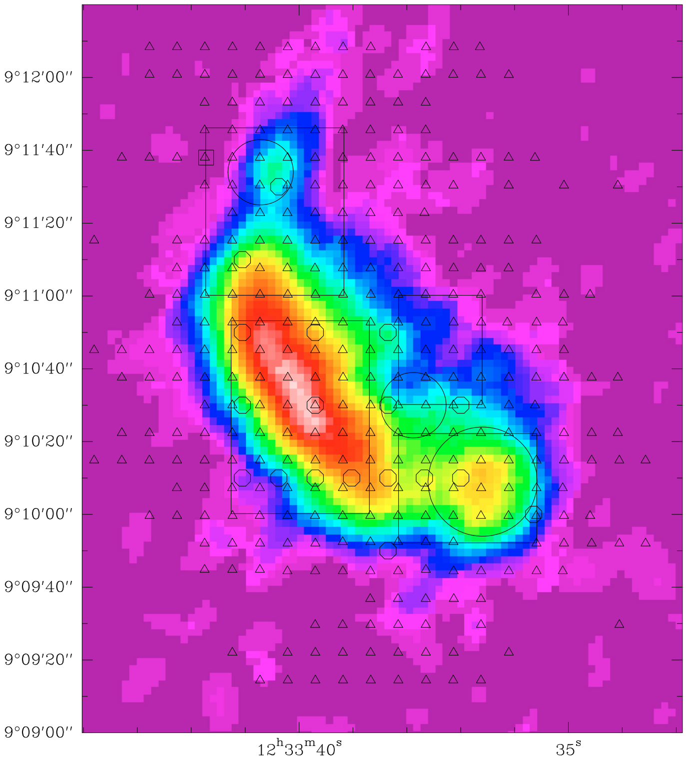

Fig. 2. ^{12}CO(2–1) HERA pointings (see Fig. 1) with low noise levels on the HI emission distribution (from Kenney et al. 2004). The large boxes correspond to Figs. 3 to 6.

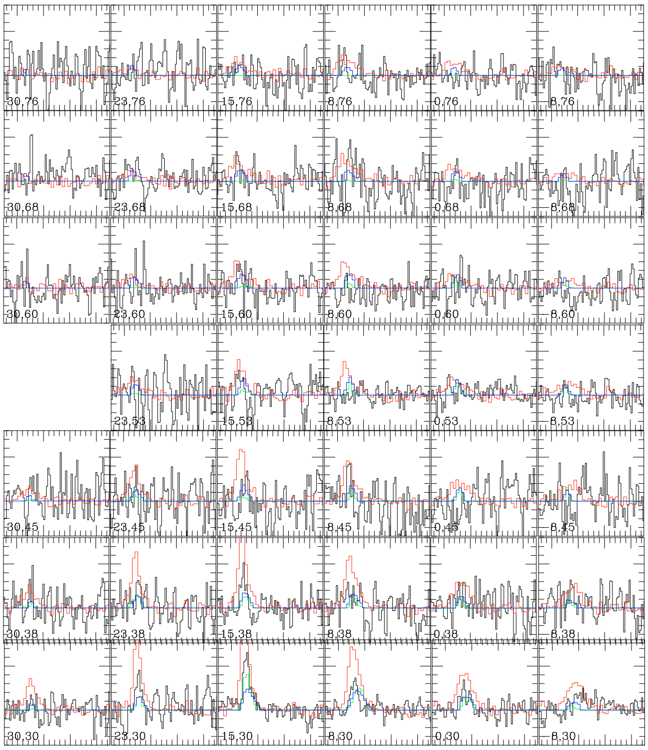

Fig. 3. IRAM 30 m HERA ^{12}CO(2–1) spectra of the northeastern box of Fig. 1 (black lines). HI spectra from Kenney et al. (2004; red lines). CO (green lines) and HI (blue lines) spectra from the dynamical model of Vollmer et al. (2006). The velocity scale is from 2150 to 2550 km s^{-1} and the main-beam temperature scale from –40 mK to 80 mK ($T_{\rm mb}$ scale).

counterpart in the CO data (Fig. 7 right panel). The CO linewidth is significantly smaller than the linewidth of the main HI line. This confirms the low molecular fraction of the blueshifted diffuse atomic gas. This blueshifted component corresponds to low surface density atomic gas discussed in Kenney et al. (2004; see their Fig. 10). The lower molecular fraction of this gas confirms the claim of Vollmer et al. (2006) that this gas has low densities making it more vulnerable to ram pressure stripping.

The ^{12}CO(1–0) spectra (resolution: 21″) are shown together with the convolved ^{12}CO(2–1) HERA spectra in Fig. 8. For all but offset (20″, 0), the CO(1–0) line closely follows the CO(2–1) line with a line ratio of 0.7–0.9. Thus, the density and temperature of the molecular gas in the western extraplanar regions is probably not significantly different from those of the molecular gas in the galactic disk. At the eastern edge we observe a lower CO(2–1)/CO(1–0) ratio (∼0.5). Given the sharpness of the gas distribution at the eastern edge and the pointing uncertainty of the telescope at 115 GHz, this small line ratio could be due to an offset of the CO(1–0) pointing to the west, i.e. closer to the major axis, with respect to the CO(2–1) pointing.

4. Wind-decoupled molecular gas

In another Virgo spiral galaxy, NGC 4438, Vollmer et al. (2005) found CO emission not associated with any HI emission. NGC 4438 underwent a tidal interaction ∼100 Myr ago (Combes et al. 1988) and now undergoes severe ram pressure stripping (Vollmer et al. 2005). A narrow CO line was detected in the northern tidal arm of NGC 4438, with apparently no associated HI. Since the velocity of the CO line corresponds to that of the stellar component (determined using a dynamical model

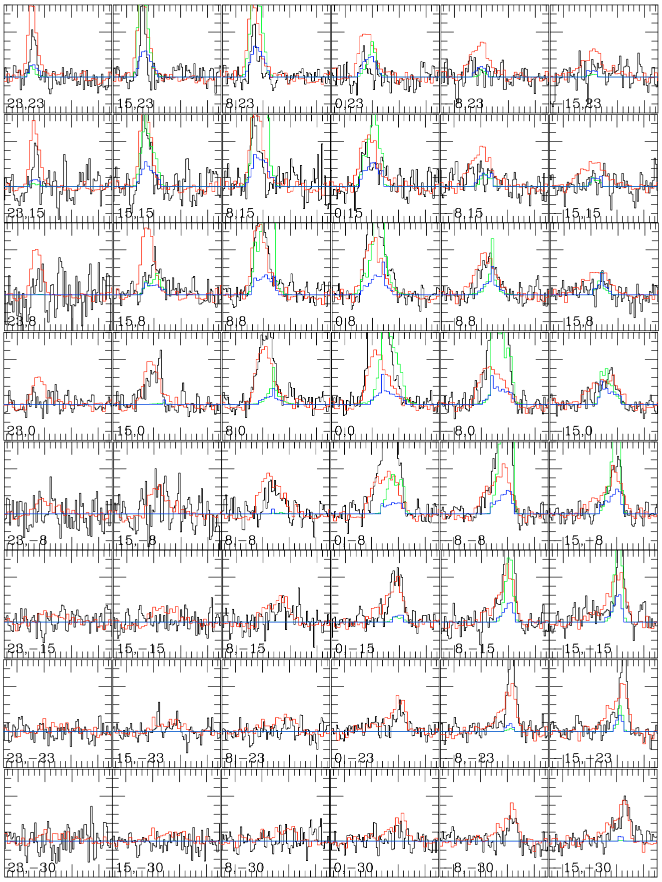

Fig. 4. Same as Fig. 3.

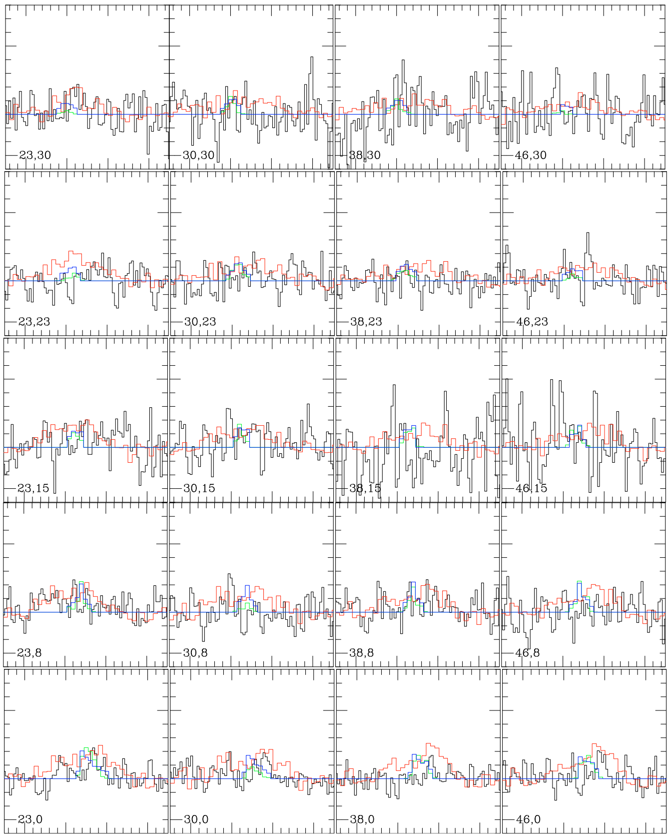

Fig. 5. Same as Fig. 3.

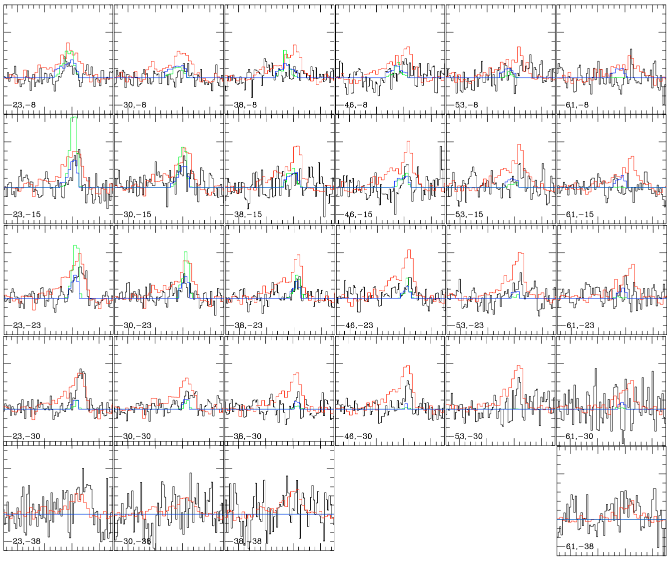

Fig. 6. Same as Fig. 3.

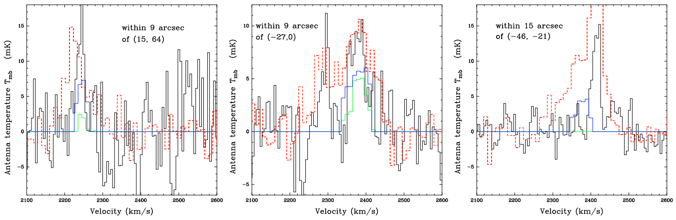

Fig. 7. Binned IRAM 30 m HERA ^{12}CO(2–1) spectra (see large circles in Fig. 1). HI spectra from Kenney et al. (2004) (red lines). CO (green lines) and HI (blue lines) spectra from the dynamical model of Vollmer et al. (2006).

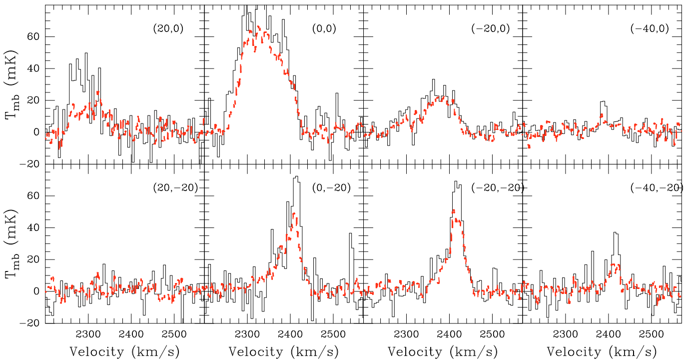

Fig. 8. Black: ^{12}CO(1–0) spectra (see small circles in Fig. 1). Red: convolved ^{12}CO(2–1) HERA spectra.

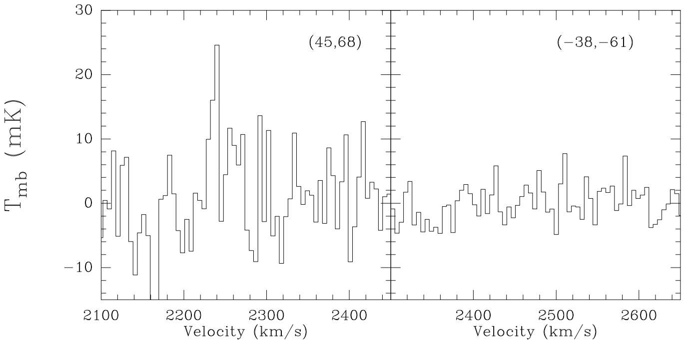

Fig. 9. Average ^{12}CO(2-1) spectra of the northeastern (45, 68) and the southwestern (−38, −61) ends of the galactic disk, where the atomic hydrogen has been removed by ram pressure. No HI emission is detected nor does the model predict any gas. The spectra are averaged over a region of 20″.

of the tidal interaction), Vollmer et al. (2005) claimed that these molecular clouds were too dense to be affected by ram pressure, i.e. that they decoupled from the ram pressure wind.

Based on these findings we searched for CO lines in regions devoid of any HI emission: (i) in the ram pressure stripped outer galactic disk (Fig. 9); and (ii) between the northern galactic disk and the extraplanar HI emission (Fig. 10). We only detect one CO line in the northern part of the galactic disk. The most prominent CO line is detected at the position (30, 68); see the little box in Figs. 1 and 2), i.e. between the stellar disk and the stripped extraplanar atomic gas. The radial velocity of the CO lines is ~2250 km s^{-1}, close to the velocity of the stellar component. The HI line of the stripped extraplanar HI (Fig. 3) is blueshifted by ~30 km s^{-1}. We observe a clear absence of a CO line in the gas-free southwestern part of the disk (Fig. 9 right panel), for which an explanation is proposed in Sect. 6.1.

5. Comparison with the dynamical model

In this section we will compare the molecular gas and Hα distribution to the dynamical model of Vollmer et al. (2006).

5.1. Molecular gas

In order to estimate the H$_2$ column density distribution, via a zero moment (integrated intensity) map of the CO(2–1) emission, we proceed as below. For the positions where the S/N of the HI is higher than 2.5σ, the linewidths of the HI spectra of these positions are determined and the CO spectra integrated over the

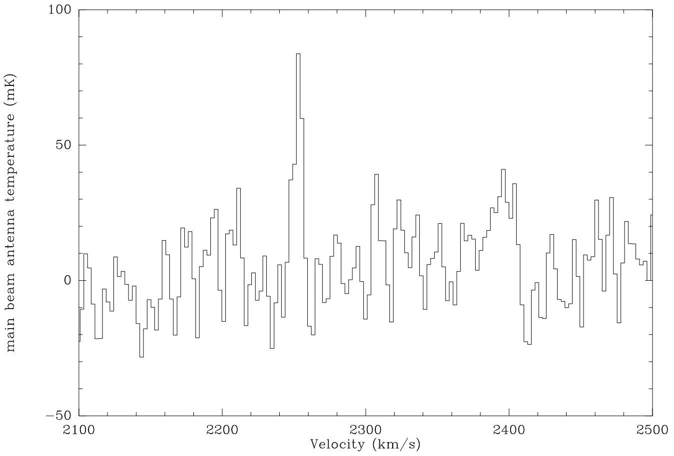

Fig. 10. Single ^{12}CO(2–1) HERA spectrum in the northeast that is located outside the HI distribution. The position is marked with an additional box in Fig. 2.

HI velocity range. This leads to the CO emission distribution map of Fig. 11 (top panel).

To compare the HI and the CO emission distributions with the dynamical model of Vollmer et al. (2006), we assume that the molecular fraction of the gas depends on the local gas density. In a first simple approach we assume that the gas is bimodal, i.e. entirely molecular at densities $>0.03\ M_\odot\ \mathrm{pc}^{-3} = 1\ \mathrm{cm}^{-3}$ and entirely atomic at lower gas densities. The resulting model gas distribution maps were convolved to the observational resolutions (middle panel of Fig. 11). In a second approach we assume that the molecular fraction depends linearly on the square root of the gas density $f_{\mathrm{mol}} = \sqrt{\rho/(0.5\ M_\odot\ \mathrm{pc}^{-3})}$. Moreover, the molecular fraction cannot exceed unity. In Sect. 6.2 we will give a motivation for this dependency. The resulting model CO emission distribution is shown in the lower panel of Fig. 11.

The comparison between the observed and the simulated CO emission distribution shows the following similarities:

- the galactic disk is the most prominent feature. There is more molecular gas of higher surface densities in the outer part of the gas disk in the southwest than in the northeast;
- there is CO emission in the extraplanar regions;
- the model using a molecular fraction proportional to the square root of the gas density better reproduces the CO morphology of the extraplanar regions: the northern and southwestern CO emission regions are centered on the peaks of the HI emission and there is a spatially separated CO arm between the southwestern and the disk CO emission.

On the other hand, we observe the following disagreement between the model and our observations:

- the model CO emission distribution shows a central hole. This is due to the initial conditions which had an initial gas hole for computational reasons;
- the northern part of the observed CO disk shows emission of lower surface brightness. The HI emission (Kenney et al. 2004) shows the opposite trend: high column density gas is found to the north;
- the model CO emission to the west of the galaxy center is more extended than it is observed. This is also the case for the HI emission (see Sect. 6).

We thus conclude that the model reproduces qualitatively our CO observations. The model using a density-dependent molecular fraction reproduces the observations better than a bimodal molecular fraction.

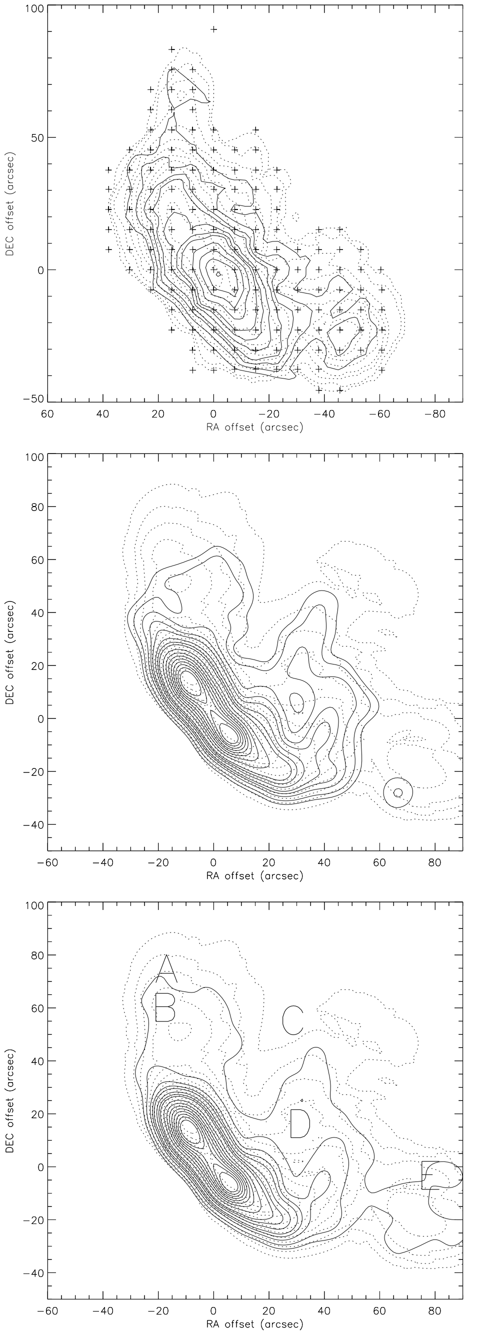

Fig. 11. *Top panel*: ^{12}CO(2–1) emission distribution (solid line) on the HI emission distribution (dotted line). The plus signs show the IRAM HERA pointings which were used to construct the CO moment 0 map. *Middle panel*: model CO distribution (solid line) on the model HI emission distribution (dotted line). The gas is assumed to be entirely molecular for gas densities $\rho > 0.03\ M_\odot\ \mathrm{pc}^{-3}$. *Lower panel*: model CO distribution (solid line) on the model HI emission distribution (dotted line). The molecular gas fraction is calculated using $f_{\mathrm{mol}} = \sqrt{\rho/(0.5\ M_\odot\ \mathrm{pc}^{-3})}$. The letters refer to the regions shown in the deprojection in Fig. 14.

The direct comparison between the HI and CO model and observed spectra (Figs. 3 to 7) shows good agreement for high intensities, i.e. high gas densities. However, the observed CO and HI double lines and blueshifted wings of the HI lines in the western extraplanar regions are not reproduced by the model.

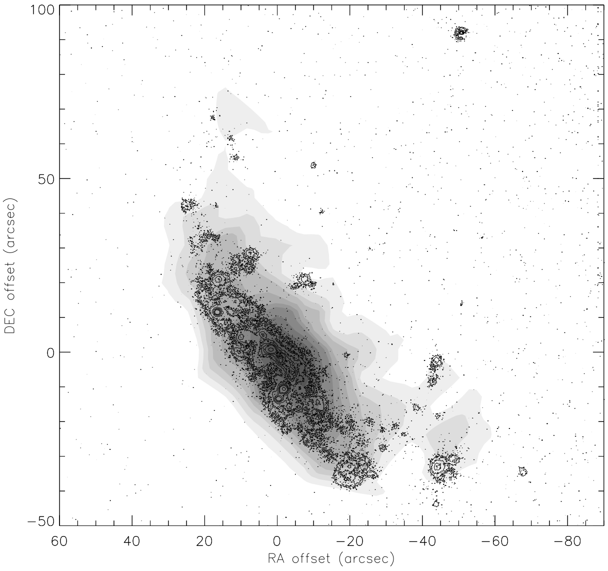

Fig. 12. Hα emission distribution (Kenney et al. 2004; contours) on the ^{12}CO(2–1) emission distribution (greyscale).

This is due to the constant column density of the model gas in the regions affected by ram pressure (see Sect. 6).

5.2. Star formation

In typical spiral galaxies the star formation rate follows more closely the molecular gas distribution than the atomic gas distribution (Wong & Blitz 2002). The HI surface density saturates at a value of $\sim$10 $M_\odot$ pc^{-2} or even declines for high star formation rates per unit surface. In an unperturbed galactic disk the ISM is confined in the gravitational potential of the disk. The ISM is turbulent and this turbulence is most probably maintained by the energy input from SN explosions (see, e.g. MacLow & Klessen 2004, or Vollmer & Beckert 2003). Without a constant energy supply, turbulence is damped within a few Myr (Stone et al. 1998; MacLow 1999). Since the extraplanar gas of NGC 4522 is no longer confined to the potential of the galactic disk, it represents an ideal laboratory to test if the gravitational potential plays a role for the correlation between star formation rate and the available molecular/atomic gas mass.

To do so, we first present the Hα emission distribution overlaid onto the CO emission distribution (Fig. 12). There is no major site of massive star formation without associated CO emission. At the edges and outside the galactic disk star formation does not coincide with the maxima of CO emission. A high column density of molecular gas is thus not sufficient to form massive stars. In other words, on kpc scales the star formation rate does not directly depend on the molecular gas surface density. A number of HII regions are detected at the outer edges of the CO emission distribution, at offsets (20″, 45″), (−10″, 20″), (−45″, 0), (−45″, −30″).

In the model we assume that the star formation rate is proportional to the number of collisions between the gas clouds. Numerically, the star formation rate thus depends on the local number density of the clouds, their cross section, and their local 3D velocity dispersion. Since the model clouds have a constant surface density (Vollmer et al. 2006), their cross sections vary with the cloud mass in the following way: $\pi r_{\rm cl}^2 = M_{\rm cl}/\Sigma$, where $r_{\rm cl}$ is the radius, $M_{\rm cl}$ the cloud mass and Σ the gas surface density. The cloud mass distribution is a power law with an index of −1.5. For an isolated unperturbed spiral galaxy this prescription leads to a Schmidt law of the form $\dot{\Sigma}_* \propto \Sigma^{1.7}$, where $\dot{\Sigma}_*$ is the star formation rate per area. For the construction of a star formation distribution map we store all cloud–cloud collisions during 20 Myr before the present state of the galaxy. This is twice the timescale for Hα emission, chosen to give more collisions and thus better statistics. The distribution was then convolved to 0.6 times the resolution of the CO(2–1) map. This model star formation distribution is presented in Fig. 13 together with the Hα emission distribution.

We note the following points for comparison between the model and observations:

- as in the observations, our model has two prominent HII regions at the outer edges of the galactic disk, the most prominent being the southwestern HII region. These regions are separated by a local minimum from the rest of the galactic disk;
- we observe extraplanar model star formation regions close to the disk at the edges and in the middle of the galactic disk (see Sect. 6);
- there is isolated star formation over the whole extraplanar HI emission. In the model the small patches are due to multiple collisions of a single massive cloud.

We thus conclude that the model star formation distribution qualitatively reproduces the observed Hα emission distribution.

6. Discussion

6.1. Deprojecting the model

The model gives us the unique opportunity to deproject the gas distribution. One has to keep in mind that the extraplanar gas is no longer located within the galactic disk, but is a fully 3D feature. In Fig. 14, we present a deprojected face-on view of the model gas distribution of Fig. 11 (lower panel). The corresponding regions are labeled with capital letters. Region A is the tip of a spiral arm close to the main gas disk. Region B is a large overdensity within the stripped gas. Region C represents the tip of the most prominent gas (spiral) arm which is mainly made of stripped material. Region D is a secondary gas arm and region E is an overdensity in the windward, low-density side of the prominent gas (spiral) arm. As stated above, the gas outside the main gas disk ($R < 30''$) has a fully 3D structure. As can be seen in the lower panel of Fig. 11, the upper edge of the deprojected gas distribution becomes the northeastern edge of the model distribution in the observed projection. The prominent gas (spiral) arm (D, C) runs in the observed projection vertically from the southwestern edge of the galactic gas disk to the end of the gas distribution at (40, 40) (Fig. 14). The southwestern extraplanar HI emission region is made of relatively diffuse gas from the low-density side of the prominent gas (spiral) arm. This low-density side has one overdensity (E) where star formation can proceed. This is consistent with the observed HI and Hα emission distribution, but we do not claim that this is the necessary configuration. Most interestingly, we can identify the upbending arm (south of D, C on the lower panel of Fig. 11) with a chain of observed HII regions (between ($12^{\rm h}33^{\rm m}38^{\rm s}$, $09^{\rm d}10^{\rm m}00^{\rm s}$) and ($12^{\rm h}33^{\rm m}37^{\rm s}$, $09^{\rm d}10^{\rm m}30^{\rm s}$) on the left panel of Fig. 13 and the corresponding molecular arm in Fig. 12. We think that this is a robust feature. As already stated in Sect. 5.1 the outer part of the upbending arm (Dec. offset 0″ to 40″ in the lower panel of Fig. 11) is not present in the observations. In deprojection this part of the arm is located between Dec. offsets of 20″ and 80″

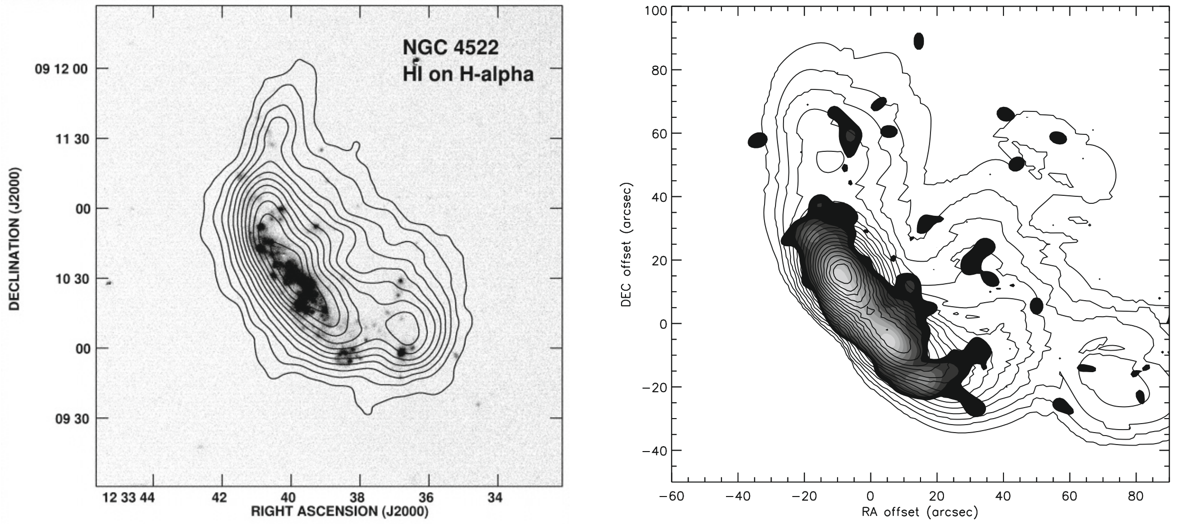

Fig. 13. *Left panel*: HI emission distribution on Hα emission distribution (Kenney et al. 2004). *Right panel*: model HI distribution (Vollmer et al. 2006; contours) on the model massive star formation distribution (greyscale). Darker regions correspond to less massive star formation.

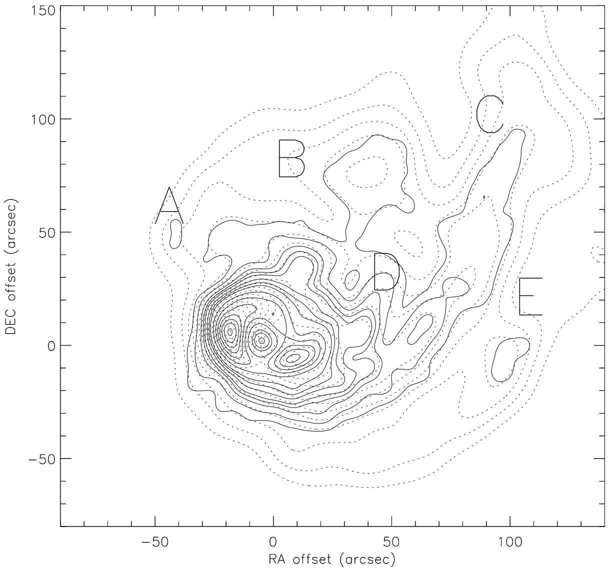

Fig. 14. Deprojected model CO distribution (solid line) on the deprojected HI distribution (dotted line). The letters correspond to the characteristic regions of Fig. 11. The galaxy is moving towards the *lower left corner* and rotates clockwise.

(Fig. 14). Due to its low total gas surface density Σ with respect to the inner part (Dec. offset $-20''$ to $0''$) it is more vulnerable to ram pressure stripping or evaporation (the acceleration a due to ram pressure p is $a = p/\Sigma$). This is consistent with the blueshift and large linewidth of the extraplanar low column density HI which is stripped more efficiently than the high column density gas (Fig. 9 of Vollmer et al. 2006). Moreover, the CO and HI spectra of the southern extraplanar HI region (Fig. 6) show that CO is only associated with high column density HI at the highest velocities. Our numerical model cannot reproduce the more efficient stripping of low column density gas, because it uses a constant column density for the atomic gas phase (see Vollmer et al. 2001 and Fig. 9 of Vollmer et al. 2006). We therefore suggest that the outer part of the stripped gas arm has been stripped more efficienctly and now has a column density too low to be detected in the HI observations. On the other hand, very dense gas can decouple from the ram pressure wind (see Sect. 4) as it is found in CO observations of NGC 4438 (Fig. 4 of Vollmer et al. 2005).

We conclude that the formation of molecular clouds and star formation mainly depend on the large-scale overdensity of the gas more than on dynamical criteria or the overall pressure (see Sect. 6.3).

Wind-decoupled molecular gas is only found in the northern part of the galactic disk (Sect. 4). With the help of the deprojection (Fig. 14), this can be understood. High density gas is stripped from the left border of the gas disk. Since the ram pressure wind is rather face-on, the gas clouds are pushed to larger heights above the galactic plane. At the same time, rotation makes clouds move towards positions A and B, i.e. the northern part of the disk where the wind-decoupled molecular clouds are found. This finding suggests that dense giant molecular clouds can decouple from the ram pressure wind at early stages of the stripping of dense gas from the galactic disk, as seems to be the case for NGC 4438 as well.

6.2. Molecular fraction

As seen in Sect. 5.1 and Fig. 11, a molecular fraction which is proportional to the square root of the total gas density reproduces the observed CO emission distribution better than a simple bimodal molecular gas fraction assuming a gas density cutoff. Vollmer & Beckert (2003) approximated the molecular fraction by the ratio between the turbulent crossing time scale $t_{\rm turb} = r_{\rm cl}/v_{\rm turb}$ and the timescale for molecule formation $t_{\rm mol} = \alpha/\rho_{\rm cl}$, where $v_{\rm turb}$ is the turbulent velocity dispersion within the cloud, $\rho_{\rm cl} = \rho/\Phi_{\rm V}$ the cloud density, ρ the total large-scale gas density, $\Phi_{\rm V}$ the volume filling factor, and α the constant of molecule formation $\alpha \sim 3 \times 10^7$ yr $M_{\odot}$ pc^{-3}:

$$f_{\rm mol} = \frac{t_{\rm turb}}{t_{\rm mol}} = \frac{r_{\rm cl}\,\rho}{v_{\rm turb}\,\alpha\,\Phi_{\rm V}}\,. \qquad (1)$$

The volume filling factor $\Phi_{\rm V}$ is defined by the condition that the gas clouds are self-gravitating, i.e. the turbulent cloud crossing time $t_{\rm turb}$ equals the free fall time $t_{\rm ff}$ of the clouds:

$$\frac{r_{\rm cl}}{v_{\rm turb}} = \sqrt{\frac{3\,\pi\,\Phi_{\rm V}}{32\,G\,\rho}}, \qquad (2)$$

where G is the gravitation constant. Inserting Eqs. (2) into (1) leads to

$$f_{\rm mol} = \sqrt{\frac{3\,\pi}{32\,G}}\,\alpha^{-1}\Phi_{\rm V}^{-\frac{1}{2}}\rho^{\frac{1}{2}}\ . \qquad (3)$$

Thus, the molecular fraction depends on the square root of the cloud density $\rho_{\rm cl} = \Phi_{\rm V}^{-1}\rho$. For the dependence used in Sect. 5.1 we assume a constant volume filling factor (see Vollmer & Beckert 2003). A density of 0.5 $M_{\odot}$ pc^{-3} implies a volume filling factor of $\Phi_{\rm V} = 0.03$. This is higher than the volume filling factors given in Vollmer & Beckert (2003). Equation (1) is a crude approximation which may overestimate the molecular fraction by a factor of 5–10, probably because $f_{\rm mol}$ is substantially overestimated by $t_{\rm turb}/t_{\rm mol}$. However, we think that its dependence on the physical parameters of the gas are valid. Equation (3) will be used together with a similar expression for the star formation efficiency in the next section. The observed molecular gas fraction decreases from 50% within the galactic disk to 35% in the extraplanar region (Table 1).

6.3. The efficiency of extraplanar star formation

Does the star formation efficiency (SFE) change once the gas has left the confining gravitational potential of the galactic disk? The role of large-scale processes in provoking star formation is subject to debate, with many "recipes" providing reasonably similar fits to observations – e.g. the "Toomre" criterion (Kennicutt 1989), a pressure-based criterion (Blitz & Rosolowsky 2006), or a basic Schmidt (1959) law. The problem is not so much predicting the behavior in spiral disks but understanding what governs large-scale star formation in general in order to be able to understand other environments, typically those at intermediate and high redshifts. In classical dwarf galaxies, it is difficult to study the SFE because the low metallicity makes the measure of the H_2 mass uncertain. In Tidal Dwarf Galaxies, morphologically similar but with higher metallicities, Braine et al. (2001) found that, curiously, the SFE was not identifiably different from spiral galaxies typically 100 times more massive. In the post-collision Taffy galaxies or UGC 813/816 system, on the other hand, the SFE in the bridge gas is much lower than within spiral disks (Braine et al. 2003, 2004).

The SFE can be defined with respect to the molecular gas mass available or with respect to the total gas mass available, either ${\rm SFE}^{-1} = t_{\rm H_2}^{\rm SFR} = M({\rm H_2})/\dot{M}_{\rm SFR}$ or ${\rm SFE}^{-1} = t_{\rm tot}^{\rm SFR} = M({\rm H_2 + HI})/\dot{M}_{\rm SFR}$. The observed gas masses, molecular fractions and star formation rates and timescales are presented in Table 1. Whereas close to half of the HI is found beyond the galactic disk, this ratio decreases to 1/4 for the molecular gas and to 1/7 for the Hα emission. The averaged star formation timescale based on the molecular or total gas mass increases from 2.2 or 4.7 Gyr within the galactic disk to 5.3 or 15.3 Gyr respectively within the extraplanar region. The star formation efficiency thus decreases by a factor of ~3 between the disk and the extraplanar region.

In the framework of the model of Vollmer & Beckert (2003) the local star formation rate is given by

$$\dot{\rho}_{*} = \Phi_{\rm V}\frac{\rho}{t_{\rm ff}^{\rm cl}}, \qquad (4)$$

Table 1. Derived masses, molecular fractions, and star formation rates/timescales.

	Galactic disk	Extrapl.	Total	Frac. extrapl.
$M_{\rm HI}\left(10^8\ M_{\odot}\right)$	2.5	1.5	4	0.4
$M_{\rm H_2}\left(10^8\ M_{\odot}\right)$	2.2	0.8	3	0.25
$M_{\rm H_2}/M_{\rm HI}$	0.88	0.53	0.75	
SFR $\left(M_{\odot}\ {\rm yr}^{-1}\right)$	0.1	0.015		~0.14
$t_{\rm H_2}^{\rm SFR}$ (Gyr)	2.2	5.3		
$t_{\rm tot}^{\rm SFR}$ (Gyr)	4.7	15.3		

where $\Phi_{\rm V}$ is the probability of finding a self-gravitating cloud, i.e. the volume filling factor of self-gravitating clouds. Inserting the expression for the free fall time of Eq. (2) into Eq. (4) yields the following expression for the star formation timescale which corresponds to the inverse of the star formation efficiency:

$$t_{*} = \frac{\rho}{\dot{\rho}_{*}} = \sqrt{\frac{3\,\pi}{32\,G}}\,\Phi_{\rm V}^{-\frac{1}{2}}\rho^{-\frac{1}{2}}. \qquad (5)$$

Thus, the star formation timescale depends on the inverse of the square root of the total large-scale density and the volume filling factor.

From Table 1 we obtain:

$$\frac{f_{\rm mol}^{\rm disk}}{f_{\rm mol}^{\rm ext}} = 1.3\ ,\ \ {\rm and}\ \ \frac{t_{*}^{\rm ext}}{t_{*}^{\rm disk}} = 3.3, \qquad (6)$$

leading to

$$\frac{\Phi_{\rm V}^{\rm disk}}{\Phi_{\rm V}^{\rm ext}} = 2.5\ ,\ \ {\rm and}\ \ \frac{\rho_{\rm disk}}{\rho_{\rm ext}} = 4.3. \qquad (7)$$

We therefore suggest that the observed decrease of the star formation efficiency by a factor of 3 in the extraplanar region, together with a lower molecular fraction, is due to a higher volume filling factor of self-gravitating clouds in the galactic disk of NGC 4522. These clouds are about twice as dense as their counterparts in the extraplanar regions. The overall density in the extraplanar region is about 4 times lower than that of the galactic disk, presumably because the extraplanar gas is no longer confined by the gravitational potential of the disk. This is supported by the lower CO(2–1)/(1–0) line ratio in the extraplanar gas (Fig. 8). However, the gas is still confined by the hot intracluster medium and partially compressed by ram pressure. The mixture of ram-pressure and rotation create zones where the atomic gas is dense enough to be gravitationally bound, become molecular, and form stars.

We conclude that the stripped ISM still forms molecules and stars in a way not distinguishable from disk star formation (Eqs. (1) and (4)) as long as the overall gas density is high enough to form bound clouds. The ultimate fate of the stripped gas is probably ionization and evaporation, without star formation for the low-density gas, and after a generation of stars, which then disperse the remaining dense gas, for the initially denser gas.

As the simulations show (Fig. 14) part of the gas is stripped in relatively dense arms whose mean density is about 4 times lower than that of the galactic gas disk. Since these gas arm are only confined by the hot intracluster medium, they might ultimately disperse giving rise to a large low surface density tail as observed in NGC 4388 (Oosterloo & van Gorkom 2005).

6.4. Comparison with radio continuum observations

Recently, Murphy et al. (2008a,b) compared Spitzer 24 μm emission with 20 cm radio continuum maps. The radio-FIR correlation is used to predict the radio emission from the Spitzer 24 μm

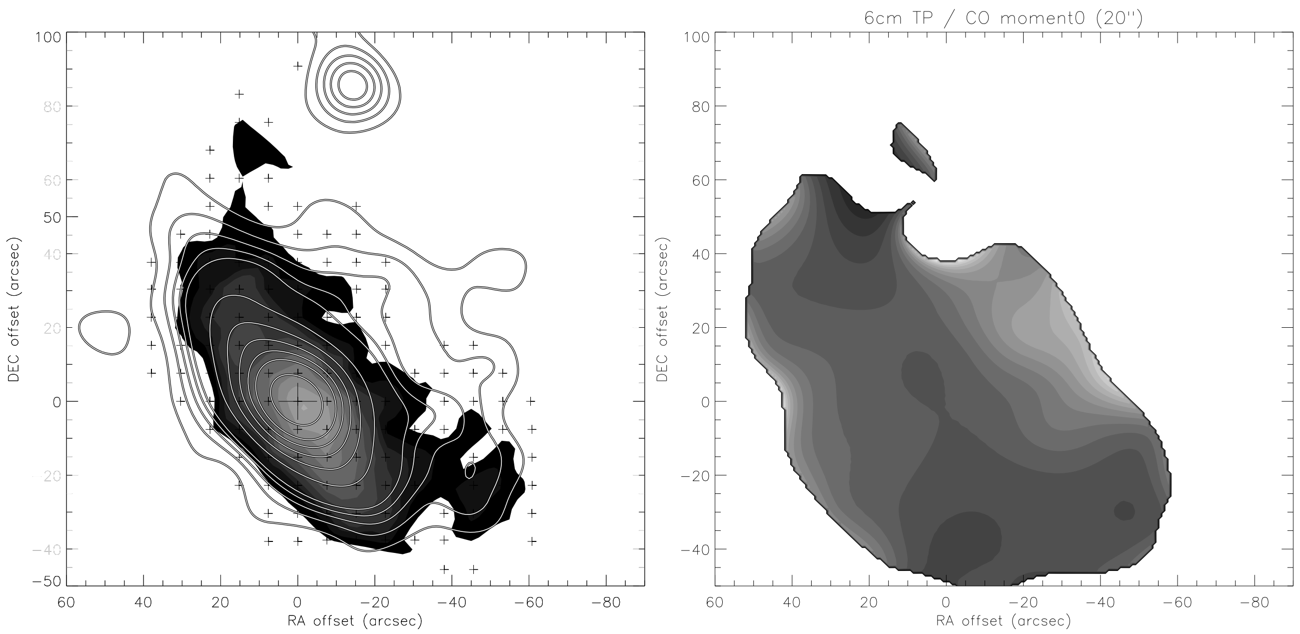

Fig. 15. *Left panel*: contours of the 6 cm radio continuum emission from Vollmer et al. (2004) on the CO emission distribution (greyscale). The contour levels are (2, 4, 6, 8, 10, 20, 30, 40, 50, 60, 80, 100) × 20 μJy/beam. The resolution is $15'' \times 15''$. *Right panel*: ratio between the 6 cm and CO emission. Brighter regions have higher CO/6 cm ratios.

emission. They found a radio deficient region at the eastern outer edge of NGC 4522's disk where ram pressure is pushing the interstellar medium. Since the 24 μm dust emission is associated with molecular gas, we compare in Fig. 15 the 6 cm radio continuum emission from Vollmer et al. (2004) with the CO emission distribution. The extraplanar 6 cm radio continuum emission extends farther to the west than the CO emission. The radio emission of the northeastern disk extends in the region where we found CO emission without associated HI emission (Fig. 9). The northern extraplanar CO and HI emission does not show associated radio continuum emission. We convolved the 6 cm radio continuum and CO maps to a resolution $20''\times20''$ and computed a ratio map which is shown in the right panel of Fig. 9. As expected, the 6 cm/CO ratio is highest in the extraplanar region. The smallest 6 cm/CO ratios are found at the extremities of the disk. We observe a maximum of the 6 cm/CO at the eastern edge of the galactic disk where Murphy et al. (2008a,b) detect a radio deficient region. Since we do not expect the 24 μm emission to be proportional to the CO emission, the interpretation of the result is difficult. In addition, we think that our data are not sensitive enough to draw a firm conclusion on the 6 cm/CO ratio map.

7. Conclusions

We present IRAM 30 m ^{12}CO(2–1) HERA and ^{12}CO(1–0) observations of the ram pressure stripped Virgo spiral galaxy NGC 4522. We directly compare the CO spectra to the HI data cube of Kenney et al. (2004). In a second step a CO emission distribution map is produced in the regions where HI is detected. The CO emission distribution is compared to Hα observations of Kenney et al. (2004) and to the model distribution of molecular gas derived from dynamical simulations of Vollmer et al. (2006). A map of the distribution of star formation based on the numerical cloud-cloud collisions is produced which is then compared to the Hα emission distribution. The 3D model snapshot allows us to deproject the observed features and understand their origin. From this work we conclude that:

1. CO emission is associated with the extraplanar atomic gas. The morphology of the molecular gas closely follows but is less extended than the HI morphology.
2. In the northern part of the galactic disk we find CO emission without an HI counterpart. We interpret this detection as wind-decoupled molecular clouds as observed in NGC 4438 (Vollmer et al. 2005).
3. In the extraplanar region CO emission is always associated with sites of massive star formation as probed by Hα emission. At the resolution of our observations, there is no correlation between the CO and Hα peaks.
4. A model using a molecular fraction proportional to the square root of the gas density qualitatively reproduces our CO observations.
5. The model star formation distribution, which is numerically based on cloud–cloud collisions, qualitatively reproduces the observed Hα emission distribution.
6. The deprojection of the model extraplanar gas shows that a significant part of the gas is stripped in the form of relatively dense arms.
7. The formation of molecular clouds, and subsequent star formation, occurs at peaks in the large-scale volume density of the gas, with no clear difference with respect to the disk despite the very different conditions (i.e. stellar density dominates in the disk but is negligible in the extraplanar material).
8. In the disk gas, the molecular and atomic fractions are about equal whereas in the extraplanar gas, there is twice as much HI as H_2, assuming a standard $N(H_2)/I_{CO}$ conversion ratio.
9. The star formation efficiency of the extraplanar gas is about 3 times lower than that of the galactic disk.
10. Using the analytical framework of Vollmer & Beckert (2003) we find that the overall total gas density and volume filling factor of self-gravitating clouds are factors of 4 and 2.5 lower respectively compared to the galactic disk.

In the early phases of ram pressure stripping (~50 Myr after peak ram pressure; Vollmer et al. 2006) a significant part of the stripped gas is in the form of relatively dense arms. At the same time some very dense molecular clouds, representing a tiny fraction of the stripped gas, can decouple from the ram pressure wind. Molecules and stars form within the stripped dense gas according to the same laws as in the galactic disk, i.e. they mainly depend on the overall total gas density. Star formation proceeds where the local large-scale gas density is highest. Given the complex 3D morphology this does not necessarily correspond to the peaks of the surface density. In the absence of a confining gravitational potential these stripped gas arms will most probably disperse, i.e. their density will decrease and star formation will cease.

Acknowledgements. Based on IRAM observations. IRAM is supported by INSU/CNRS (France), MPG (Germany), and IGN (Spain). We made use of a DSS image. The Digitized Sky Survey was produced at the Space Telescope Science Institute under US Government grant NAG W-2166. The images of these surveys are based on photographic data obtained using the Oschin Schmidt Telescope on Palomar Mountain and the UK Schmidt Telescope. The plates were processed into the present compressed digital form with the permission of these institutions.

References

Blitz, L., & Rosolowsky, E. 2006, ApJ, 650, 933
Braine, J., Duc, P.-A., Lisenfeld, U., et al. 2001, A&A, 378, 51
Braine, J., Davoust, E., Zhu, M., et al. 2003, A&A, 408, L13
Braine, J., Lisenfeld, U., Duc, P.-A., et al. 2004, A&A, 418, 419
Combes, F., Dupraz, C., Casoli, F., & Pagani, L. 1988, A&A, 203, L9
Crowl, H. H., & Kenney, J. D. P. 2006, ApJ, 649, L75
Helou, G., Hoffman, G., & Salpeter, E. E. 1984, ApJS, 55, 433
Kenney, J. P. D., & Koopmann, R. A. 1999, AJ, 117, 181
Kenney, J. P. D., van Gorkom, J., & Vollmer, B. 2004, AJ, 127, 3361
Kennicutt, R. C., Jr. 1989, ApJ, 685, 344
MacLow, M.-M. 1999, ApJ, 524, 169
MacLow, M.-M., & Klessen, R. S. 2004, RvMP, 76, 125
Murphy, E., Kenney, J., Helou, G., Chung, A., & Howell, J. 2008a, ApJ, submitted
Murphy, E. J., Kenney, J. D. P., Helou, G., et al. 2008b, eprint [`arXiv:0802.2281`]
Oosterloo, T., & van Gorkom, J. H. 2005, A&A, 437, L19
Schmidt, M. 1959, ApJ, 129, 243
Stone, J. M., Ostriker, E. C., & Gammie, C. F. 1998, ApJ, 508, L99
Vollmer, B., & Beckert, T. 2003, A&A, 404, 21
Vollmer, B., Beck, R., Kenney, J. P. D., & van Gorkom, J. H. 2004, AJ, 127, 3375
Vollmer, B., Braine, J., Combes, F., & Sofue, Y. 2005, A&A, 441, 473
Vollmer, B., Soida, M., Otmianowska-Mazur, K., et al. 2006, A&A, 453, 883
Wong, T., & Blitz, J. 2002, ApJ, 569, 157